Chapter 7

Numerical Reconstruction Results

In this chapter we present results that were obtained with the MOBIIR scheme based on the ERT using synthetically generated measured data. First, we compared the performances of the BFGS, lm-BFGS, and CG methods. We show reconstruction results of μ_s for different *signal-to-noise ratios* (SNR) and different initial guesses μ_{s_0}. Second, reconstruction results of μ_s for different numbers of source-detector pairs are presented. In addition, we show a reconstruction example of a medium that contained a void region.

7.1 Comparison of BFGS, lm-BFGS, and CG Methods

The main focus of our study was the comparison of computational speed, robustness, and accuracy of the BFGS, lm-BFGS, and CG methods in OT. Therefore, we compared these techniques for different signal-to-noise ratios of the measurement data and for different initial guesses. Various SNR change the appearance of the objective function and subsequently lead to different reconstruction results. Furthermore, starting the optimization process from different initial guesses may also lead to different reconstruction results. The objective function may have a single local minimum, but the line search pro-

ceeds on different paths towards the minimum that can lead to a premature termination if the stopping criterion is satisfied. Moreover, if the starting point is too far away from the true solution, the quadratic model may not be a good approximation of the objective function. Consequently, the line search does not proceed towards the minimum at all.

7.1.1 Problem Set-up and Method

An example of a scattering medium is shown in Figure 7.1. The cross-sectional image to be reconstructed consisted of three objects with scattering coefficients of $\mu_s = 2.9$ cm^{-1}, $\mu_s = 8.7$ cm^{-1}, and $\mu_s = 11.6$ cm^{-1}, which were embedded in a 3 cm $\times$ 3 cm background medium with $\mu_s = 5.8$ cm^{-1}. The absorption coefficient $\mu_a = 0.35$ cm^{-1} did not vary within the isotropically scattering medium ($g = 0$). The general character of the objective function primarily depends on the data type used (e.g. data in the time domain, frequency domain, or in the continuous wave domain) [Schweiger99], and is independent of the physical properties of the tissue-like medium. Therefore, various examples with different optical parameters will not lead to fundamentally different results, and the same study could also have been carried out for anisotropically scattering media or for various absorption coefficients. Indeed we have simulated different types of media that vary in absorption and scattering properties. The results were qualitatively the same as for that presented in this example.

The medium was surrounded by 8 equally spaced sources and 116 equally spaced detectors. 2 sources and 29 detectors were placed on each side of the medium. Detector readings on the same side as the source, were not used for the reconstruction. Hence, we obtained a total of 8×87 source-detector pairs. The measured data at the detector positions were generated by using the correct spatial distribution of optical properties (see Figure 7.1). The forward calculations were performed on a 61×61 grid with 16 ordi-

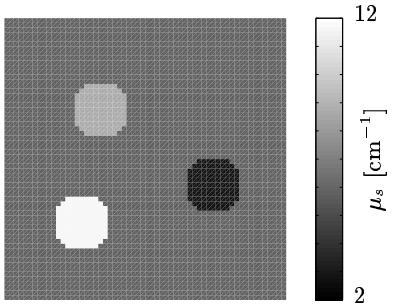

Figure 7.1: Scattering coefficients μ_s of original medium with dimensions of 3 cm × 3 cm containing three heterogeneities ($\mu_s = 2.9$ cm^{-1}, $\mu_s = 8.7$ cm^{-1}, and $\mu_s = 11.6$ cm^{-1}). The bulk medium had a scattering coefficient of $\mu_s = 5.8$ cm^{-1}.

nates by using the finite-difference discrete-ordinates method based on the ERT. We used partly reflective boundary conditions based on Fresnel's law with a homogeneous refractive index $n = 1.54$ for the scattering medium. The synthetic measurement data were used to reconstruct an image of the distribution of μ_s. The reconstruction process was terminated after the relative difference $|(\Phi_{k+1} - \Phi_k)/\Phi_k|$ of the objective function between two subsequent iteration steps k and (k+1) was smaller than $\epsilon = 10^{-3}$. This stopping criterion replaced the criterion $\|\nabla\Phi(\boldsymbol{\mu}_k)\| < \epsilon$ as mentioned in Subsection 5.2.4. The gradient $\nabla\Phi(\boldsymbol{\mu}_k)$ contained very large values in proximity to source positions, which contributed more to the overall norm $\|\nabla\Phi(\boldsymbol{\mu}_k)\|$ than the remaining vector elements. Therefore, the condition $|(\Phi_{k+1} - \Phi_k)/\Phi_k| < \epsilon$ appears to be better suited for our applications.

7.1.2 Definition of Image Accuracy

For evaluating the image accuracy of the reconstructed images, we determined the *correlation coefficient* $\rho_a \in [-1, 1]$ of the reconstructed image and the original medium (target image). This coefficient is defined as [Press92]

$$\rho_a = \frac{\sum_i^{I \cdot J} (\mu_{s_i}^r - \bar{\mu}_s^r)(\mu_{s_i}^t - \bar{\mu}_s^t)}{(I \cdot J - 1)\Delta\mu_s^r \Delta\mu_s^t}, \tag{7.1}$$

where the *standard deviation* $\Delta\mu_s^t$ of the target medium and the standard deviation $\Delta\mu_s^r$ of the reconstructed image are given by

$$\Delta\mu_s^t = \sqrt{\frac{1}{\mathrm{I}\cdot\mathrm{J}-1}\sum_{\mathrm{i}}^{\mathrm{I}\cdot\mathrm{J}}(\mu_{s_\mathrm{i}}^t - \bar{\mu}_s^t)^2} \tag{7.2}$$

and

$$\Delta\mu_s^r = \sqrt{\frac{1}{\mathrm{I}\cdot\mathrm{J}-1}\sum_{\mathrm{i}}^{\mathrm{I}\cdot\mathrm{J}}(\mu_{s_\mathrm{i}}^r - \bar{\mu}_s^r)^2}. \tag{7.3}$$

The index $\mathrm{i} \in [1, \mathrm{I}\cdot\mathrm{J}]$ constitutes one pixel of the image or one element of the vector $\boldsymbol{\mu}_s$, respectively. The quantities $\bar{\mu}_s^t$ and $\bar{\mu}_s^r$ indicate the *mean values* of optical parameters of the target image and the reconstructed image, respectively. A large value of ρ_a shows a high correlation between the reconstructed and the target image and indicates a reconstructed image with high accuracy. Almost no correlation between the target and the reconstructed image is found if ρ_a is very small.

Besides the correlation coefficient ρ_a, we also define a *deviation factor* $\rho_b \in [0, \infty)$ as:

$$\rho_b = \frac{\sqrt{1/(\mathrm{I}\cdot\mathrm{J})\sum_{\mathrm{i}}^{\mathrm{I}\cdot\mathrm{J}}(\mu_{s_\mathrm{i}}^r - \mu_{s_\mathrm{i}}^t)^2}}{\Delta\mu_s^t}. \tag{7.4}$$

This parameter is a measure of the deviation of the reconstructed image from the target image. It is defined as the ratio of the χ-square error norm, which was obtained from the target and reconstructed image, and the standard deviation of the target image. A small value of ρ_b indicates a reconstructed image with high accuracy. The correlation coefficient and the deviation factor of all reconstructed images of the numerical study are shown in Table 7.1 on page 122.

7.1.3 Impact of Noise

The detector readings, obtained from an experimental setting, are always corrupted by noise. In our numerical study we determined the affects of different noise levels

based on the assumption that only shot noise [1] from the source (laser diode) is the dominant noise contribution throughout the measurement process. Therefore, we defined the noise level σ_{m_d} as the standard deviation of the *Gaussian distribution* around the signal m_d of the d-th source-detector pair of the measurement vector $\boldsymbol{m}$. The SNR of the measurement data in units of dB is obtained from:

$$\mathrm{SNR} = 10 \log_{10} \frac{m_\mathrm{d}}{\sigma_{m_\mathrm{d}}}. \tag{7.5}$$

We found previously that the SNR of our experimental set-up was within 15 dB to 25 dB (see Chapter 4). Given that range of SNR we determined the noise level or standard deviation σ_{m_d} from Equation 7.5. Subsequently, a Gaussian distributed random number was calculated [Press92] using this standard deviation σ_{m_d}. A new noise-corrupted measurement value was obtained by adding this random number to the measurement value m_d.

We carried out the numerical study on four examples with different SNR present in the synthetic measurement data (no noise, 45 dB SNR, 20 dB SNR, and 15 dB SNR) using the test medium as explained in Subsection 7.1.1. First, no noise was added to the synthetic measurements. We reconstructed the scattering coefficients μ_s starting from an initial guess μ_{s_0} that had the same optical parameters as the background medium. The reconstruction was performed using the CG method, lm-BFGS method, and the BFGS method. The objective functions of all three methods are depicted in Figure 7.2(a). The value of the objective function is displayed as a function of the number of basic operations. A basic operation is either a forward or a gradient calculation. Since the time of a forward calculation is nearly the same as that of one gradient calculation, the abscissa can be

[1] Shot noise is the time-dependent fluctuation in electrical current associated with the discreteness of the charge carrier in semiconductor devices. The charge carriers create photons by recombination processes in laser diodes. Since noise represents randomly fluctuating events, we must use statistical distributions to characterize noise. When the photon numbers are large a continuous probability distribution such as the Gaussian distribution is needed.

interpreted as the execution time of the optimization process. Furthermore, we define the number of iterations as the number of derivative calculations.

As can be seen in Figure 7.2(a) the lm-BFGS method reached the stopping criterion after 92 basic operations, which consisted of 54 forward and 38 gradient calculations (54+38)[2]. The BFGS method converged after 172 basic operations (98+74). The CG method took the longest time to reach the stopping criterion, requiring 395 basic operations (363+32). The absolute number of forward runs and gradient calculations differed, depending on the method used. Usually the CG method made more forward runs and fewer gradient calculations than the QN methods, because the CG method used an exact line search (line-minimization, see Subsection 5.2.1). The BFGS method and the lm-BFGS method used an inexact line search (backtracking method, see Subsection 5.2.1), which required less forward runs for each search direction. The final value $\tilde{\varphi}$ of the objective function was different for all three methods. The BFGS method had the smallest value $\log_{10}(\tilde{\varphi}) = -5.32$, whereas the CG method had the largest value $\log_{10}(\tilde{\varphi}) = -4.48$.

The resulting image reconstructions of μ_s without noise are displayed in Figure 7.3. The interval between adjacent isolines is $\mu_s = 1$ cm^{-1}. The image accuracy is highest (ρ_a is highest and ρ_b is smallest) for the image obtained by the BFGS method ($\rho_a^{\mathrm{BFGS}} > \rho_a^{\mathrm{lm-BFGS}} > \rho_a^{\mathrm{CG}}$ and $\rho_b^{\mathrm{BFGS}} < \rho_b^{\mathrm{lm-BFGS}} < \rho_b^{\mathrm{CG}}$), see also Table 7.1.

Another method of comparison is to look at the reconstruction results after the same number of basic operations, which implies the same computational time. These results are shown in Figure 7.4. In this figure we present the images obtained after 92 basic operations for each method. This number was selected because it is the number of steps needed for the fastest method (lm-BFGS) to satisfy the stopping criterion. Thus, the lm-BFGS image was obtained after 38 iterations (54+38), the BFGS image after 46 iterations

[2] From now on we will write the number of forward and gradient calculations within parentheses (forward calculations + gradient calculations).

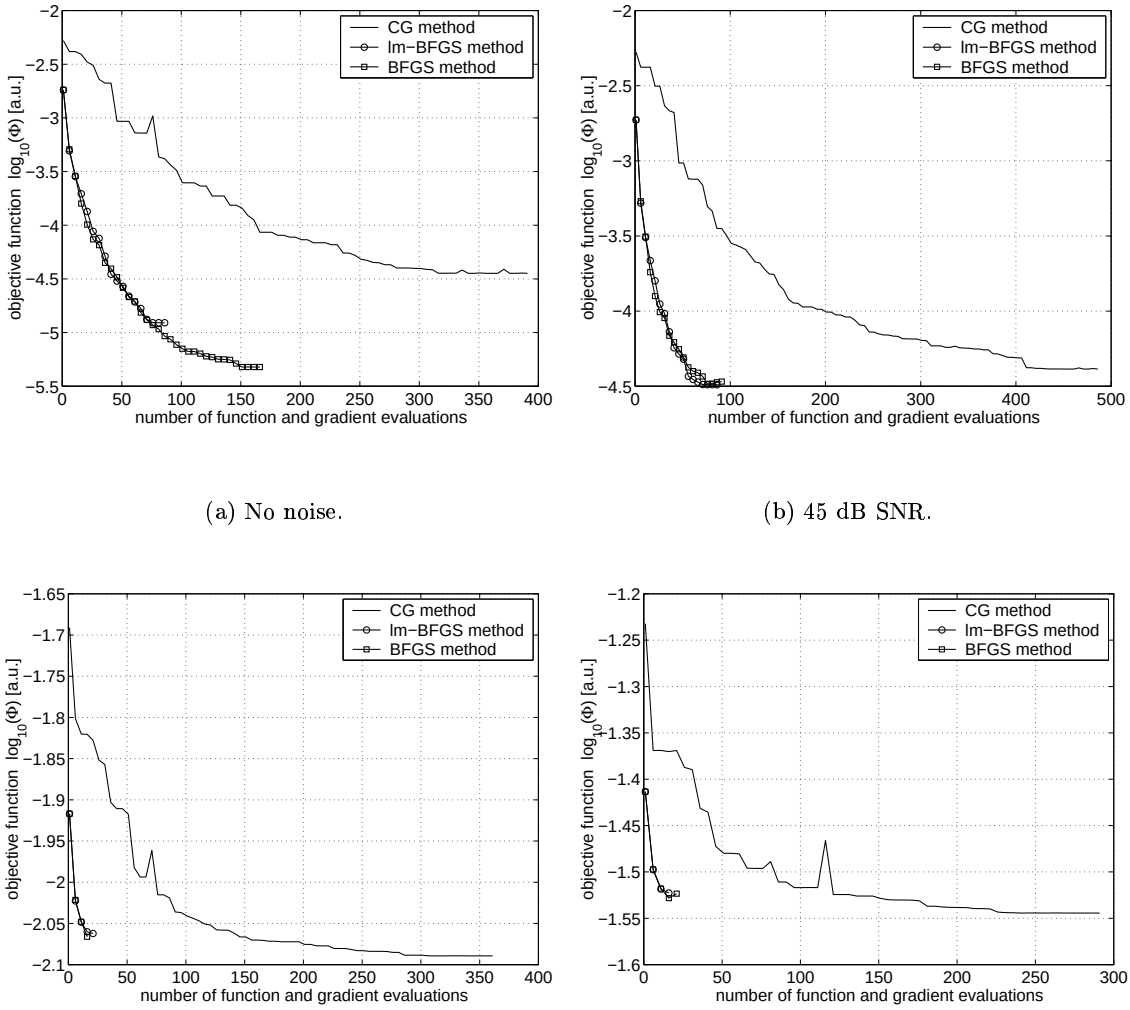

(a) No noise.

(b) 45 dB SNR.

(c) 20 dB SNR.

(d) 15 dB SNR.

Figure 7.2: Objective functions for different signal-to-noise ratios of the synthetic measurement data.

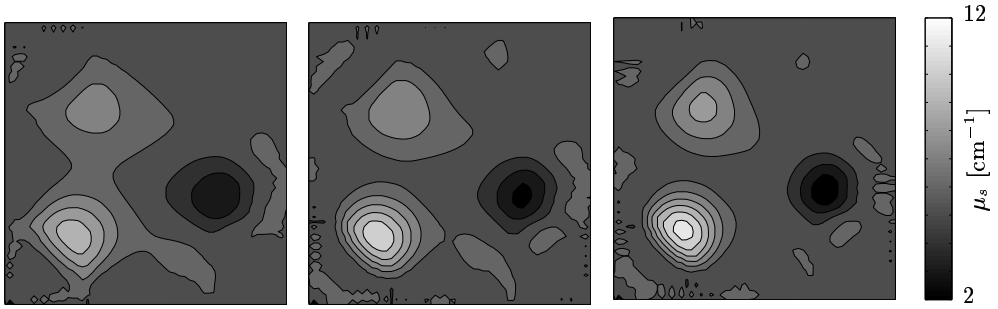

(a) CG method, after 395 basic operations.

(b) lm-BFGS method, after 92 basic operations.

(c) BFGS method, after 172 basic operations.

Figure 7.3: Final image reconstructions of μ_s. No noise was present in the synthetic measurement data. Distance between adjacent isolines is 1 cm^{-1}.

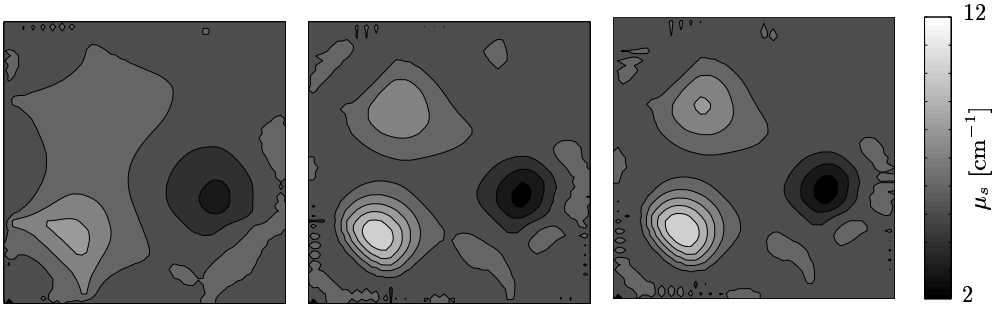

(a) CG method, after 92 basic operations (7 iterations).

(b) lm-BFGS method, after 92 basic operations (38 iterations).

(c) BFGS method, after 92 basic operations (46 iterations).

Figure 7.4: Image reconstructions of μ_s after 92 basic operations. No noise was present in the synthetic measurement data. Distance between adjacent isolines is 1 cm^{-1}.

(46+46), and the CG image after 7 iterations (85+7).

We did the same study for a second example, where we added little noise to the synthetic measurement data resulting in a SNR of 45 dB. The objective functions are shown in Figure 7.2(b). The lm-BFGS method needed 91 basic operations (55+36), and the BFGS method took 98 basic operations (54+44). The CG method took 495 basic operations (454+41) for completion. The final values after termination are $\log_{10}(\tilde{\varphi}) = -4.48$ for the BFGS and lm-BFGS method, and $\log_{10}(\tilde{\varphi}) = -4.38$ for the CG method.

The SNR of the third example was 20 dB, which is typically encountered when performing experiments on tissue (see Chapter 4). The objective functions of all three optimization techniques are presented in Figure 7.2(c), and the image reconstructions are shown in Figure 7.5. The image accuracy is highest for both the lm-BFGS and BFGS method (see Table 7.1). The final reconstructions were obtained by using the lm-BFGS method after 26 basic operations (15+11) and by using the BFGS method after 23 basic operations (12+11). The CG method took 365 basic operations (343+22) for completion. The final value of the objective function was $\log_{10}(\tilde{\varphi}) = -2.07$ for the BFGS method and lm-BFGS method, and $\log_{10}(\tilde{\varphi}) = -2.08$ for the CG method. In Figure 7.6 we show reconstructed images of all three methods for the same number of basic operations. In this case, the BFGS method was the fastest method satisfying the stopping criterion with 23 basic operations and 11 iterations. Equivalently, the lm-BFGS method needed 10 iterations for the same amount of basic operations. The CG method completed only 1 iteration. As can be clearly seen, the image accuracy is highest for the images obtained by the QN methods (see Table 7.1).

In a fourth example we decreased the SNR of the synthetic measurement data to 15 dB. The BFGS method needed 27 basic operations (15+12). The lm-BFGS method took 22 basic operations (12+10). The CG method demanded the most computational time for

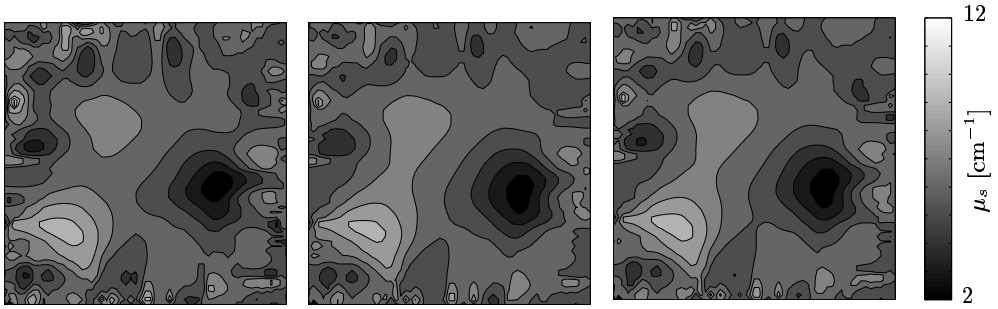

(a) CG method, after 365 basic operations.

(b) lm-BFGS method, after 26 basic operations.

(c) BFGS method, after 23 basic operations.

Figure 7.5: Final image reconstructions of μ_s. The SNR of the synthetic measurement data was 20 dB. Distance between adjacent isolines is 1 cm^{-1}.

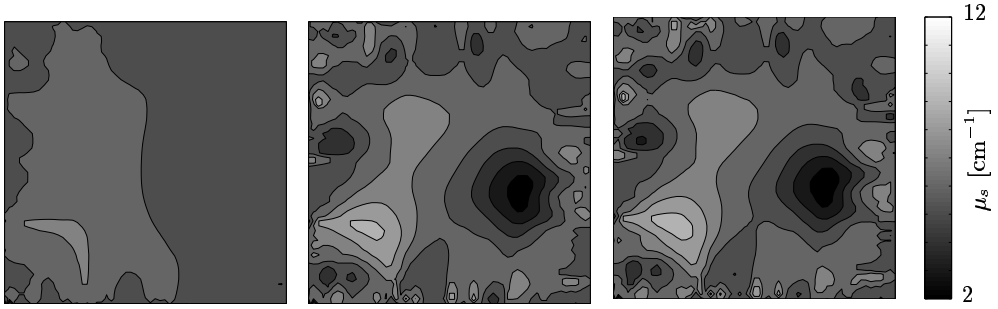

(a) CG method, after 23 basic operations (1 iteration).

(b) lm-BFGS method, after 23 basic operations (10 iterations).

(c) BFGS method, after 23 basic operations (11 iterations).

Figure 7.6: Image reconstructions of μ_s after 23 basic operations. The SNR of the synthetic measurement data was 20 dB. Distance between adjacent isolines is 1 cm^{-1}.

completion. The optimization process was terminated after 297 basic operations (281+16). The objective functions are shown in Figure 7.2(d) with the final values $\log_{10}(\tilde{\varphi}) = -1.53$ for the BFGS and lm-BFGS method and $\log_{10}(\tilde{\varphi}) = -1.54$ for the CG method.

7.1.4 Impact of Different Initial Guesses

We also studied the influence of different homogeneous initial guesses μ_{s_0}. We have chosen three different examples of μ_{s_0} with a 20%, 30% and 50% higher scattering coefficient than the original medium. The objective functions of all three examples are shown in Figure 7.7.

Figure 7.7(a) shows the results of the first example where a 20% higher scattering coefficient for the initial guess was chosen. The QN methods were faster than the CG method, and also reached a smaller value $\tilde{\varphi}$ of the objective function when the stopping criterion was satisfied. The BFGS method needed 148 basic operations (87+61) and the lm-BFGS method completed after 150 basic operations (89+61) with $\log_{10}(\tilde{\varphi}) = -5.12$ and $\log_{10}(\tilde{\varphi}) = -5.05$, respectively. The CG method took the longest requiring 398 basic operations (366+32) with $\log_{10}(\tilde{\varphi}) = -4.4$.

The second example with a 30% higher scattering coefficient (see Figure 7.7(b)) shows basically a similar result as the first example. The lm-BFGS method needed 84 basic operations (51+33) with $\log_{10}(\tilde{\varphi}) = -4.42$ to converge. The BFGS method converged after 213 basic operations (126+87) with the smallest value of $\log_{10}(\tilde{\varphi}) = -5.25$ compared to the other techniques. The CG method took the longest time to satisfy the stop criterion. It finished after 421 basic operations (389+32) with $\log_{10}(\tilde{\varphi}) = -4.25$. The final reconstructed images are shown in Figure 7.8. Additionally, we also compared all three methods after 84 basic operations, the point at which the lm-BFGS method was the first to satisfy the stopping criterion. The lm-BFGS method yielded after 33 iterations the image in Figure 7.9(b)

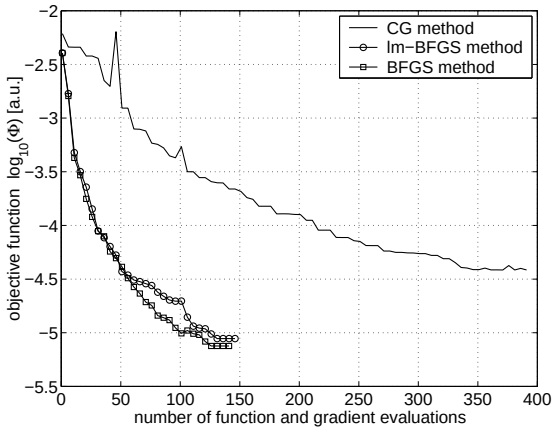

(a) Initial guess μ_{s_0} was 20% higher than the background scattering of the original medium.

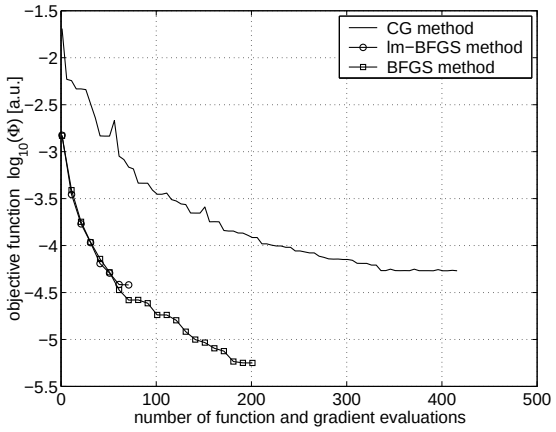

(b) Initial guess μ_{s_0} was 30% higher than the background scattering of the original medium.

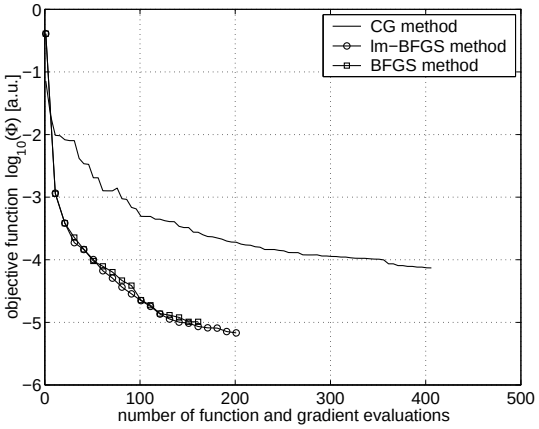

(c) Initial guess μ_{s_0} was 50% higher than the background scattering of the original medium.

Figure 7.7: Objective functions for different initial guess μ_{s_0}.

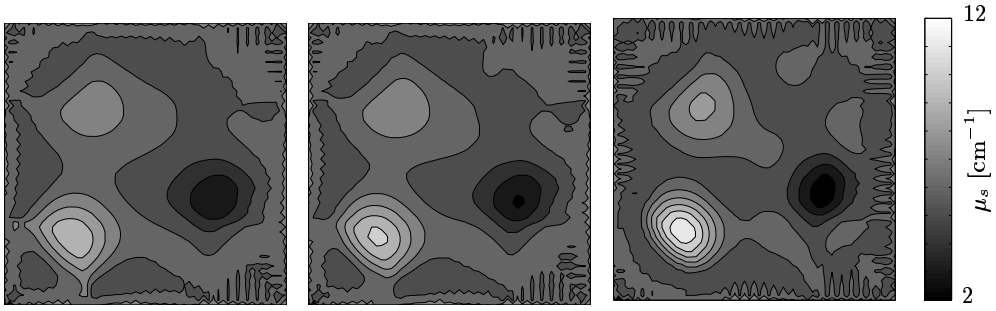

(a) CG method, after 421 basic operations.

(b) lm-BFGS method, after 84 basic operations.

(c) BFGS method, after 213 basic operations.

Figure 7.8: Final image reconstructions of μ_s. Initial guess μ_{s_0} was 30% higher than the background scattering of the original medium. Distance between adjacent isolines is 1 cm^{-1}.

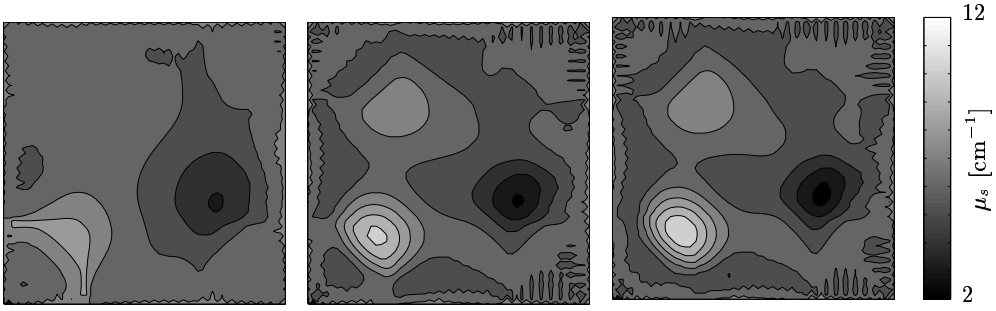

(a) CG method, after 84 basic operations (6 iterations)

(b) lm-BFGS method, after 84 basic operations (33 iterations)

(c) BFGS method, after 84 basic operations (40 iterations)

Figure 7.9: Image reconstructions of μ_s after 84 basic operations. The initial guess μ_{s_0} was 30% higher than the background scattering of the original medium. Distance between adjacent isolines is 1 cm^{-1}.

and the BFGS method needed 40 iterations and yielded the image seen in Figure 7.9(c). The CG method took 6 iterations as seen in Figure 7.9(a). The BFGS method achieved reconstructed images with the highest image accuracy (ρ_a was highest and ρ_b was smallest), see also Table 7.1.

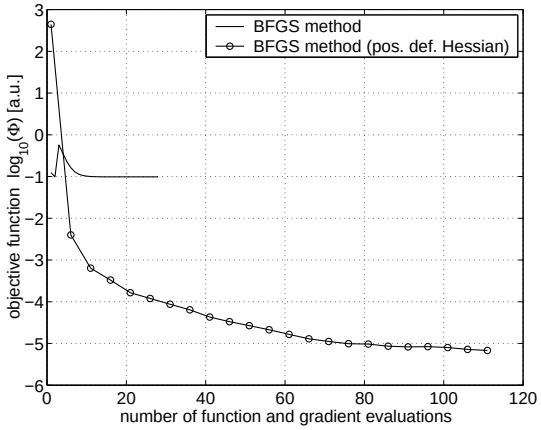

Figure 7.10: Objective functions using the BFGS method with/without a positive definite inverse Hessian. An initial guess 50% higher than the background scattering of the original medium led to a Hessian that was not positive definite.

The last example used a starting point μ_{s_0} with a 50% higher scattering coefficient (see Figure 7.7(c)). The lm-BFGS method needed 175 basic operations (98+77). The BFGS method finished after 217 basic operations (118+99). The CG technique took the longest time to reach the stop criterion. It finished after 412 basic operations (381+31). The final values of the objective function were $\log_{10}(\tilde{\varphi}) = -5.19$ for the BFGS method, $\log_{10}(\tilde{\varphi}) = -4.99$ for the lm-BFGS method, and $\log_{10}(\tilde{\varphi}) = -4.13$ for the CG method. This reconstruction example is of particular interest for the QN methods, because both the BFGS method and the lm-BFGS method automatically replaced the approximated inverse Hessian matrix with the identity matrix after the first iteration to prevent a premature convergence.

The quadratic model, as given by Equation 5.19, was not a good approximation

of the objective function at this initial guess. The inverse Hessian $\boldsymbol{\mathcal{H}}_{\mathrm{k}}$ at the starting point μ_{s_0} was not positive definite and the curvature condition (see Equation 5.28) was not satisfied. The optimization process of the BFGS method terminated after completing only the first iteration (see Figure 7.10). The final value of the objective function was only $\log_{10}(\tilde{\varphi}) = -1.01$. Therefore, the approximated inverse Hessian was replaced at the first iteration step with the identity matrix $\boldsymbol{\mathcal{H}}_{\mathrm{k}} = \boldsymbol{I}$ as explained in Subsection 5.2.5.

7.1.5 Impact of Noise and Initial Guess

In practice, we typically encounter the situation, where the measurement data are corrupted by noise and the initial guess is not close to the solution, e.g it does not closely match the background medium. We demonstrate the performance of all three optimization techniques by adding noise to the synthetic measurement data such that the SNR = 20 dB (see Figures 7.2(c) and 7.5). The reconstruction process was started from an initial guess μ_{s_0} that was 30% higher than the scattering coefficient of the background medium (see Figures 7.7(b) and 7.8).

The lm-BFGS method took 31 basic operations (18+13) and the BFGS method needed 41 basic operations (25+16), with $\log_{10}(\tilde{\varphi}) = -2.05$ and $\log_{10}(\tilde{\varphi}) = -2.06$, respectively. The longest reconstruction time was required by the CG method with 408 basic operations (382+26) and with $\log_{10}(\tilde{\varphi}) = -2.09$. The objective functions are shown in Figure 7.11. The reconstructed images are shown in Figure 7.12. The image accuracy was highest for the QN methods (see Table 7.1).

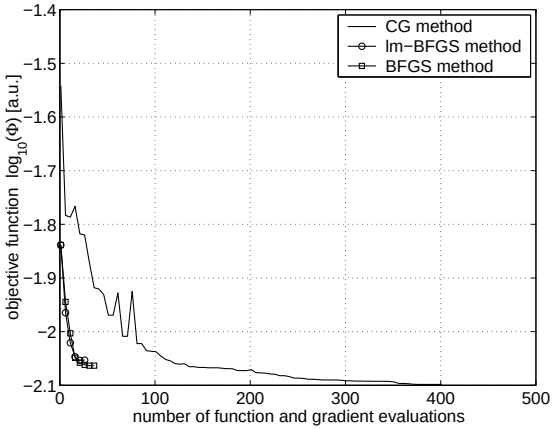

Figure 7.11: Objective functions starting from an initial guess μ_{s_0} that was 30% higher than the background scattering of the original medium. Additionally, the synthetic measurement data were corrupted by noise with a SNR of 20 dB.

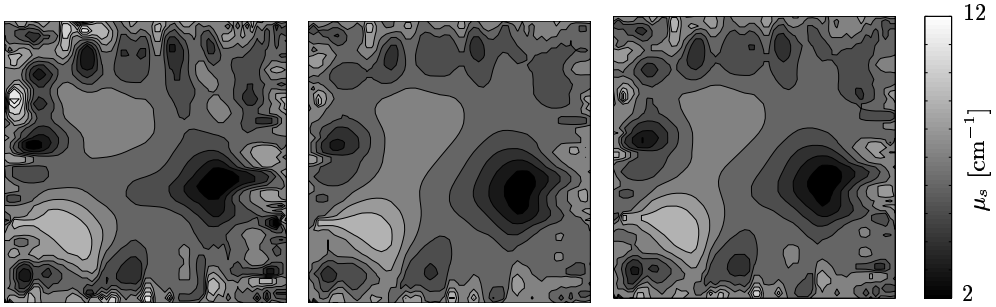

(a) CG method, after 408 basic operations.

(b) lm-BFGS method, after 31 basic operations.

(c) BFGS method, after 41 basic operations.

Figure 7.12: Final image reconstructions of μ_s. The initial guess μ_{s_0} was 30% higher than the background scattering of the original medium. The SNR of the synthetic measurement data was 20 dB. Distance between adjacent isolines is 1 cm^{-1}.

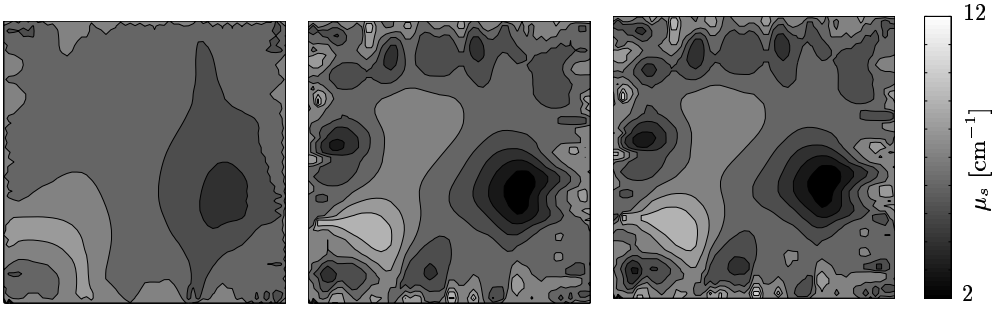

(a) CG method, after 31 basic operations (2 iterations).

(b) lm-BFGS method, after 31 basic operations (13 iterations).

(c) BFGS method, after 31 basic operations (14 iterations).

Figure 7.13: Image reconstructions of μ_s after 31 basic operations. The initial guess μ_{s_0} was 30% higher than the background scattering of the original medium. The SNR of the synthetic measurement data was 20 dB. Distance between adjacent isolines is 1 cm^{-1}.

example	number of basic operations	method	correlation coefficient ρ_a	deviation factor ρ_b
no noise	395	CG	0.80	0.62
	92	lm-BFGS	0.85	0.54
	172	BFGS	**0.87**	**0.50**
	92	CG	0.69	0.74
	92	lm-BFGS	0.85	0.54
	92	BFGS	**0.86**	**0.52**
20 dB SNR	365	CG	0.57	0.89
	26	lm-BFGS	**0.62**	**0.82**
	23	BFGS	0.61	0.83
	23	CG	0.56	0.87
	23	lm-BFGS	**0.62**	**0.82**
	23	BFGS	0.61	0.83
initial guess 30% higher	421	CG	0.72	0.72
	84	lm-BFGS	0.74	0.69
	213	BFGS	**0.82**	**0.59**
	84	CG	0.56	0.87
	84	lm-BFGS	0.74	0.69
	84	BFGS	**0.77**	**0.65**
initial guess 30% higher and 20 dB SNR	408	CG	0.45	1.24
	31	lm-BFGS	**0.55**	**1.01**
	41	BFGS	0.54	1.04
	31	CG	0.43	1.01
	31	lm-BFGS	**0.55**	**1.00**
	31	BFGS	0.54	1.02

Table 7.1: Image accuracy of reconstructed images for all three optimization techniques (CG, lm-BFGS, and BFGS). Images with highest accuracy are represented by a large ρ_a and a small ρ_b (bold-printed).

7.1.6 Discussion

Initially, we studied the impact of noise imposed on synthetic measurements. We found that the BFGS method and the lm-BFGS method lead to smaller values $\tilde{\varphi}$ of the objective function when no noise is present in the measurement data. Furthermore, the QN methods required fewer basic operations than the CG method to satisfy the stopping criterion. The CG method needed twice as many basic operations (see Figure 7.2(a)). The image accuracy, represented by the correlation coefficient ρ_a and deviation factor ρ_b, is highest for the BFGS and lm-BFGS methods (see Table 7.1).

The advantages of QN methods over CG methods were diminished once noise was added to the measurement data. All three (CG, lm-BFGS, and BFGS) methods reached approximately the same final value $\tilde{\varphi}$ of the objective function for a SNR $<$ 45dB. The image accuracy of the final reconstructed images is not significantly different. However, the lm-BFGS method and BFGS method were considerably faster than the CG method. They needed 10 to 15 times fewer basic operations than the CG method (see Figures 7.2(c) and 7.2(d)).

The QN methods also outperformed the CG method in computational speed and image accuracy when starting from different initial guesses. The CG method always needed twice as many basic operations than the QN methods. Moreover, the BFGS method and the lm-BFGS method found smaller values of $\tilde{\varphi}$ than the CG method resulting in reconstructed images with higher image accuracy (see Table 7.1). We found that the QN methods sometimes fail in calculating a search direction towards a minimum, if the initial guess μ_{s_0} of the scattering coefficient is far from the solution. In this case the approximated Hessian might not be defined or the search direction may not be a descent direction. Therefore, the Hessian matrix was automatically replaced by the identity matrix and we enforced positive-definiteness, thereby obtaining a descent search direction.

The major disadvantage of the BFGS method is its large memory requirement. Our study shows that this disadvantage can be alleviated by implementing the lm-BFGS method. The lm-BFGS algorithm requires less memory than the BFGS algorithm, while the image quality achieved with the lm-BFGS technique, was approximately equal to that obtained with the BFGS method (see Table 7.1).

In conclusion, the QN methods outperformed the CG method in the computational speed of finding the minimum of the objective function and in image accuracy. Only for measurement data with a SNR > 45dB the QN methods achieved a significant higher image accuracy and a smaller value $\tilde{\varphi}$. The QN methods needed fewer basic operations, because an approximation to the inverse Hessian for calculating the search direction and an inexact line search were used. In contrast, the CG method needed more basic operations, since it required an exact line search (line-minimization) that used more forward calculations for each gradient calculation.

7.2 Source and Detector Configuration

The objective function also depends on the number D of source-detector pairs (see Definition 5.1) and their spatial positions. Consequently, the derivative calculation also depends on the source-detector configuration, which leads to different reconstruction results of μ_s and μ_a. Hence, we performed a study on a simple test medium to estimate how many sources and detectors were necessary to yield a given image accuracy.

7.2.1 Problem Set-up and Method

We have chosen an example that contains three different scattering heterogeneities as shown in Figure 7.14. The optical parameters of the bulk medium were $\mu_{\mathrm{s}} = 11.6\ \mathrm{cm}^{-1}$, $\mu_{\mathrm{a}} = 0.35\ \mathrm{cm}^{-1}$, and $g = 0$. The three scattering perturbations had the parameters

$\mu_s = 5.8\ \text{cm}^{-1}$, $\mu_s = 17.4\ \text{cm}^{-1}$, and $\mu_s = 23.2\ \text{cm}^{-1}$. The absorption coefficient of the three perturbations was not altered.

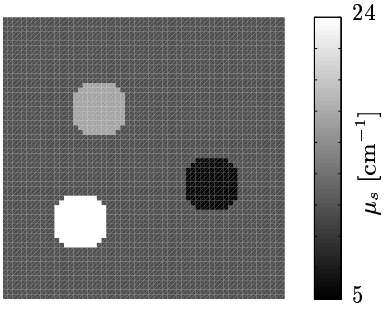

Figure 7.14: Scattering coefficients μ_s of original medium with dimensions 3 cm × 3 cm containing three heterogeneities ($\mu_s = 5.8\ \text{cm}^{-1}$, $\mu_s = 17.4\ \text{cm}^{-1}$, and $\mu_s = 23.2\ \text{cm}^{-1}$). The bulk medium had a scattering coefficient μ_s of 11.6 cm^{-1}.

7.2.2 Impact of Different Numbers of Source-Detector Pairs

For all reconstructions we used either 4, 8, or 12 sources, which were symmetrically positioned around the medium. The number of detectors consisted of sets of 12, 28, 56, or 126 that were also placed symmetrically on all four sides of the medium. Therefore, the 12 possible source-detector combinations resulted in reconstructions as shown in Figures 7.15, 7.16, 7.17, and 7.18. The grayscale of the images covers the range from $\mu_s = 5\ \text{cm}^{-1}$ to $\mu_s = 24\ \text{cm}^{-1}$. The scattering coefficient between adjacent isolines is $\mu_s = 2\ \text{cm}^{-1}$.

The image accuracy of the reconstructed images was determined by using the definitions of the correlation coefficient ρ_a (see Equation 7.1) and the deviation factor ρ_b (see Equation 7.4). The correlation coefficients and the deviation factors are given in Table 7.2. A large value of ρ_a and a small value of ρ_b indicates a high image accuracy.

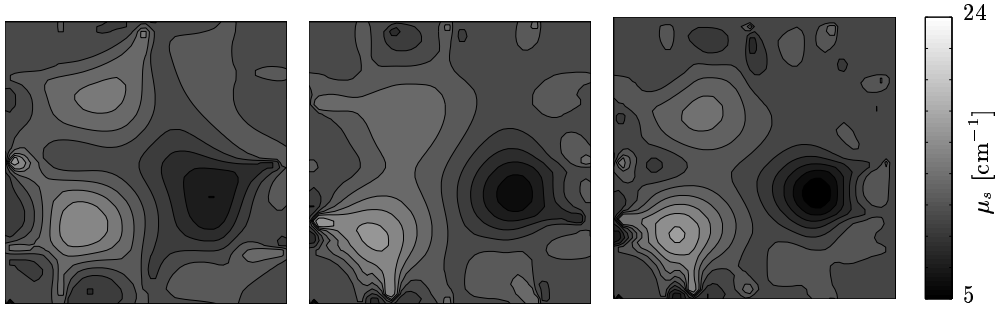

(a) 4 sources. (b) 8 sources. (c) 12 sources.

Figure 7.15: Image reconstructions of μ_s with 12 detectors. Distance between adjacent isolines is 2 cm^{-1}.

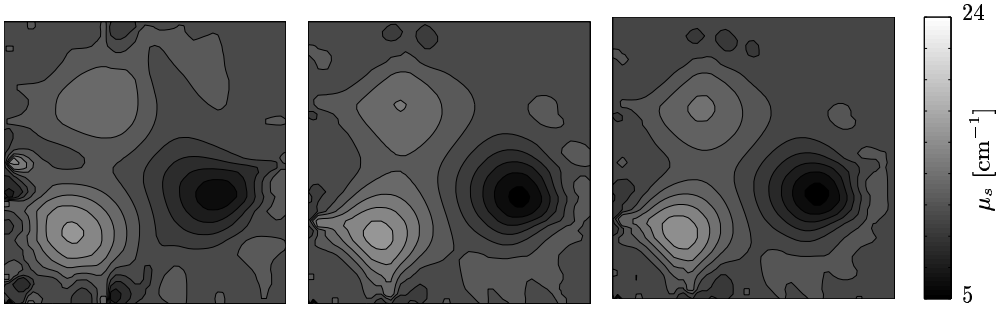

(a) 4 sources. (b) 8 sources. (c) 12 sources.

Figure 7.16: Image reconstructions of μ_s with 28 detectors. Distance between adjacent isolines is 2 cm^{-1}.

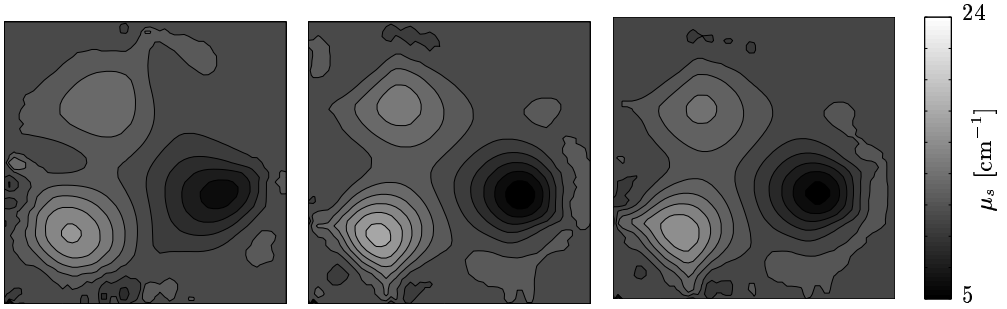

(a) 4 sources. (b) 8 sources. (c) 12 sources.

Figure 7.17: Image reconstructions of μ_s with 56 detectors. Distance between adjacent isolines is 2 cm^{-1}.

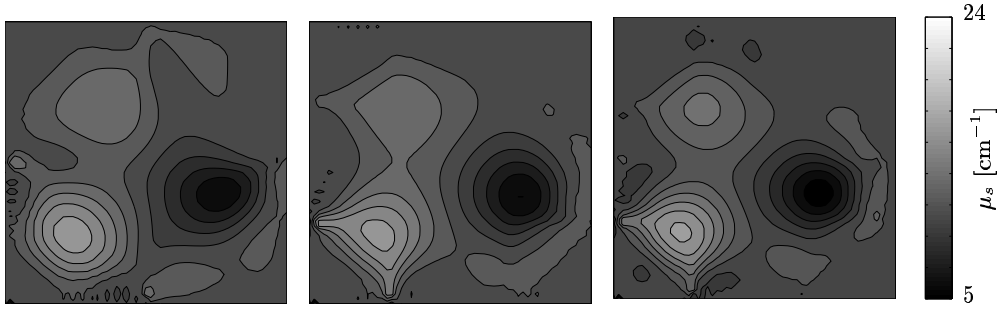

(a) 4 sources. (b) 8 sources. (c) 12 sources.

Figure 7.18: Image reconstructions of μ_s with 126 detectors. Distance between adjacent isolines is 2 cm^{-1}.

7.2.3 Discussion

Looking at Table 7.2 we found that the image accuracy increased when the number of source-detector pairs was increased from D = 4×12 (Figure 7.15(a)) to D = 8×56 (Figure 7.17(b)). A further increase in the number of source-detector-pairs did not show a significant improvement of the image accuracy. The best results were obtained with 8 sources and 56 detectors (Figure 7.17(b)), followed by 12 sources and 126 detectors (Figure 7.18(c)), and 12 sources and 56 detectors (Figure 7.17(c)).

number of source-detector pairs D	number of sources	number of detectors	correlation coefficient ρ_a	deviation factor ρ_b
48	4	12	0.62	0.79
96	8	12	0.63	0.78
144	12	12	0.70	0.72
112	4	28	0.67	0.75
224	8	28	0.70	0.73
336	12	28	0.71	0.72
224	4	56	0.70	0.74
448	8	56	**0.75**	**0.68**
672	12	56	**0.72**	**0.71**
504	4	126	0.70	0.73
1008	8	126	0.69	0.73
1512	12	126	**0.74**	**0.69**

Table 7.2: Image accuracy of reconstructed images by using different source-detector configurations. The three reconstructed images with the highest image accuracy are represented by a large ρ_a and a small ρ_b (bold-printed).

However, an absolute number of source-detector pairs, which can be applied generally to scattering media, can not be given. The number of source-detector pairs will always depend on the particular scattering medium, i.e. its optical parameters and geometrical

dimensions.

It is interesting to note that an increase in the number of detectors will not result in a larger computational time. However, increasing the number of sources increases linearly the amount of computational time needed for performing reconstructions. Therefore, it is suggested for pragmatic reasons to use the largest amount of detectors that are available for obtaining images with higher accuracy. The number of sources used is limited by the computational resources at hand.

7.3 Void Areas

In Chapter 4 we performed an experimental study on a scattering phantom that contained a void-like ring. We compared the experimental data with fluence profiles obtained with the forward model based on the ERT. However, we did not yet reconstruct the optical parameters of a void-like medium by employing the transport-theory-based MOBIIR scheme. Therefore, we generated synthetic measurement data using a numerical model of a scattering medium that contained a void-like ring. This example was similar to the phantom used in Subsection 4.1.1 for evaluating the forward model. The distribution of the scattering coefficients was reconstructed by using the synthetic measurement data of the original medium.

The test medium had dimensions of 4 cm $\times$ 4 cm and contained a ring in the center with an inner diameter of 2.4 cm and a thickness of 0.3 cm. The scattering coefficient of the background medium was $\mu_s = 58$ cm^{-1} and the the anisotropy factor was set to $g = 0.8$. The absorption coefficient was set to $\mu_a = 0.35$ cm^{-1}. The ring had a $\mu_s = 1$ cm^{-1}, $\mu_a = 0.001$ cm^{-1}, and $g = 0.8$. We placed 3 sources and 10 detectors on each side of the medium. This set-up will also be used later for experimental studies in Chapter 8.2 (see

schematic and source-detector configuration in Figure 8.3 on page 135).

We generated synthetic measurement data based on the ERT. The finite-difference grid had a size of 81×81 grid points with a grid-point separation $\Delta x = \Delta y = 0.05$ cm. We used 16 discrete ordinates and considered non-reentry boundary conditions. We started the reconstruction of μ_s by using the CG method with a homogeneous initial guess $\mu_{s_0} = 58$ cm^{-1}, $g = 0.8$, and $\mu_{a_0} = 0.35$ cm^{-1}. The reconstruction process was terminated after 334 basic operations (319+15). The reconstruction result for μ_s is displayed in Figure 7.19(b). The distance between adjacent isolines is $\mu_s = 10$ cm^{-1}.

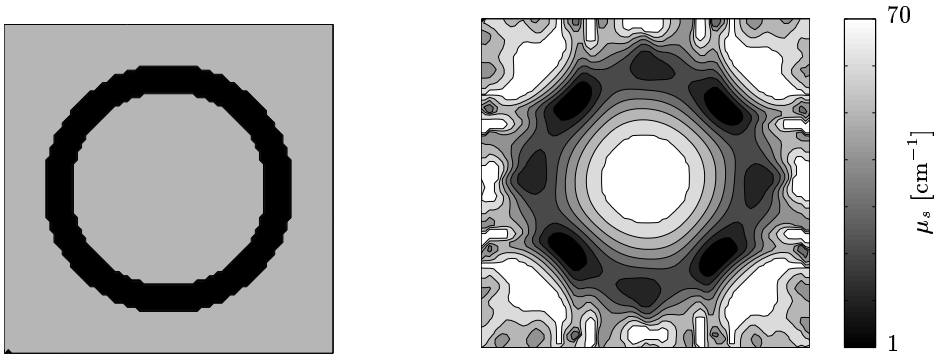

(a) Scattering coefficient μ_s of original medium.

(b) Reconstructed image of the scattering coefficient μ_s.

Figure 7.19: Original medium and reconstructed image of scattering coefficients μ_s. The original medium contained a void-like ring with $\mu_s = 1$ cm^{-1}. The bulk medium had a scattering coefficient μ_s of 58 cm^{-1}. Distance between adjacent isolines is 10 cm^{-1}.

The void-like ring is clearly visible in the reconstructed image (see Figure 7.19(b)). The smallest value of the ring is $\mu_s = 0.37$ cm^{-1}. In conclusion, the MOBIIR scheme based on the ERT is able to reconstruct void areas. Until now, this was not possible in OT by using diffusion-theory-based reconstruction methods.